

See discussions, stats, and author profiles for this publication at: <https://www.researchgate.net/publication/228508527>

Surface Segregation in Ni/Co Bimetallic Nanoparticles Produced in Single-Walled Carbon Nanotube Synthesis

ARTICLE *in* THE JOURNAL OF PHYSICAL CHEMISTRY B · JUNE 2002

Impact Factor: 3.3 · DOI: 10.1021/jp025530r

CITATIONS

26

READS

10

2 AUTHORS, INCLUDING:



Guangjun Cheng

National Institute of Standards and Technolo...

35 PUBLICATIONS 495 CITATIONS

SEE PROFILE

Surface Segregation in Ni/Co Bimetallic Nanoparticles Produced in Single-Walled Carbon Nanotube Synthesis

Guangjun Cheng and Ting Guo*

Department of Chemistry, University of California, One Shields Avenue, Davis, California 95616

Received: January 17, 2002; In Final Form: April 15, 2002

Extended X-ray absorption fine structure (EXAFS) spectroscopy and transmission electron microscopy (TEM) have been used to investigate Ni/Co bimetallic nanoparticles (bi-MNPs) in carbon species such as single-walled carbon nanotubes (SWNTs) produced via laser vaporization of a carbon–metal mixture. Results from selected area diffraction (SAD) and dark field TEM imaging measurements indicate that the structures of these nanoparticles are face-center-cubic, and energy-dispersive X-ray (EDX) elemental analysis shows that each of the nanoparticles examined contains $50 \pm 5\%$ of Ni and Co. The average coordination numbers of the nearest neighbors for Ni and Co in the bi-MNPs derived from the EXAFS data are 10.0 and 11.0, respectively. The squares of disorders (σ^2) for the Co and Ni in those nanoparticles are 0.0053 and 0.0054. The former is slightly lower than that of the Co bulk, 0.0059, whereas the latter is identical to the value for the Ni bulk. Using these coordination numbers and assuming that all the nanoparticles are in the bimetallic form, their average size is estimated to be 3 nm, much smaller than the 8-nm average size obtained from the TEM measurements. A detailed analysis of the EXAFS data using Fourier filtering and single scattering theory has revealed that the surface of the nanoparticles is predominantly occupied by Ni atoms.

Introduction

Catalysts made of bimetallic nanoparticles are superior compared with those made of pure metals, in terms of activity, selectivity, stability, and resistance to poisoning.¹ For example, bimetallic nanoparticles (bi-MNPs) are preferred heterogeneous catalysts in petroleum reforming processes.² Large diameter bi-MNPs have been used to catalyze the growth of carbon filaments.³ Recently, Ni/Co bimetallic species have been used to produce high yields of single-walled carbon nanotubes (SWNTs);^{4–6} the yield of the SWNTs so produced increases by more than 10 times in comparison to their monometallic counterparts.

The magic of bi-MNPs usually originates from their structures. Many investigations have shown that the structure–function relationship involving these nanoparticles holds the key to the understanding of catalytic processes. For instance, the catalytic mechanisms of monometallic nanoparticles (mono-MNPs) and bi-MNPs in petroleum refining processes and multiwalled nanotube production are understood only after the structures of these catalysts have been determined.^{2,5} In one of the thoroughly investigated cases, bi-MNPs have been examined by Sinfelt and colleagues with extended X-ray absorption fine structure (EXAFS) techniques. Among the systems they have studied, they have found that Cu atoms concentrate in the surface of Ru/Cu bi-MNPs.² Such segregation helps reduce the rate of hydrogenolysis, which requires large patches of Ru atoms to function. Pd–Pt bimetallic systems have also been investigated by many groups, and these bi-MNPs are known to be more resistive to sulfur poisoning due to the special surface arrangement.^{8,9,1} These results clearly demonstrate that special structures of bi-MNPs can lead to novel properties and enhancement of activities such as the catalytic function.

Although no direct evidence has been found linking SWNT diameter sized bi-MNPs ($\sim 1.6 \pm 0.5$ nm) to the end of nanotubes in such cases as laser vaporization and arc discharge of metal–graphite composite targets, possibly due to the extreme fast rates of SWNT formation under these conditions, these nanoparticles are believed to be responsible for the growth of SWNTs for the following reasons. First, mono-MNPs have been found at the end of many SWNTs synthesized in various slow-growing environments, including chemical vapor deposition (CVD) and a specially designed, two-step laser vaporization process.⁷ Second, under the same conditions, the yield of SWNTs is generally much higher when two metals instead of one are used. For example, two metals, Ni and Co, can act collectively, albeit nonadditively to greatly enhance the yield of SWNTs. If the two metals stay apart from each other, no such enhancement should occur.

Numerous reports have been published on the growth mechanisms of SWNTs, from both theoretical and experimental perspectives.^{10–23} To date, a great wealth of experimental data on these nanoparticles is available, including that on the overall composition, size distribution, and crystallinity.^{24,25} Furthermore, experimental results have shown that the composition of MNPs can alter the yield and diameter of SWNTs. However, little attention has been paid to the detailed structural features such as surface composition of the relevant nanoparticles, and more of such critical pieces of information are needed to help fully understand the catalytic growth mechanisms. As a result, the exact role of MNPs is still largely unknown.²⁶

To address the question of why the alloying Ni/Co bi-MNPs are better catalysts, we have investigated these particles produced in a laser vaporization apparatus. We wish to demonstrate that at least those particles synthesized at the optimized temperature of 1200 °C possess unique structures when they are cooled to room temperature. This finding may

* Corresponding author. E-mail: tguo@ucdavis.edu.

prove important to understanding the greatly enhanced yield of SWNTs so produced.

Experimental Section

Samples containing SWNTs, amorphous carbon, and bi-MNPs were obtained from *tube@rice*.²⁷ They were the raw material produced by laser vaporization of a composite target made of graphite and micron-sized powders of metallic Ni and Co. The concentrations of Co and Ni metals in the composite target were both ca. 0.6 at. %. We chose to examine the product from laser vaporization because it was in this case that Ni and Co together catalyzed the production of SWNT at a much higher yield than the two metals did alone, which indicated that these materials possessed certain properties that differed from a simple mixture of the two.

EXAFS measurements, which probe the immediate chemical environment around an absorbing element in composite materials and are ideal to studying bi-MNPs, were performed on the K edges of Ni and Co in both Ni/Co bi-MNPs and the standards, which were Ni and Co thin foils (3- μm thickness). Raw soot of a few micrograms containing both webs of SWNTs and bi-MNPs was examined. The experiments were performed at the beamline 4-1 at the Stanford Synchrotron Radiation Laboratory (SSRL) with a double silicon crystal (220) monochromator. Harmonics were suppressed by detuning the crystal spectrometer. No efforts were made to control the temperature of the samples. EXAFS data was obtained by detecting the fluorescence of K lines from Ni and Co in the bi-MNP samples using a Lytle detector. Simultaneously, transmission mode detected with ion chambers was employed to acquire the EXAFS data on the standards. In fluorescence mode, thin metal foil filters placed in front of the Lytle detector were used to reduce the scattering of incident X-rays by the sample and sample holder. Mn and Fe filters were used when detecting Co and Ni fluorescence, respectively.

To reduce the amount of interference of Co fluorescence to the Ni EXAFS data in the near edge region, we also used a LN₂-cooled, 13-element, high-energy resolution (300-eV fwhm) Ge detector to replace the Lytle detector. The parameters of each element of the detector were optimized separately.

EXAFS Analyses

The EXAFS data was collected using the XAS program at SSRL. Data analysis was performed using ATOMS, EXAFSPAK, and FEFF7.²⁸ The subtraction of polynomial fit preedge and spline-fit atomic absorption curves, and k^3 factor multiplication were all built-in in the EXAFSPAK package. The processed EXAFS data in k reciprocal space was directly obtained from that in the energy space using $k = \sqrt{2m(E-E_0)}$. A 3.5–11 \AA^{-1} k range was used for processing the EXAFS data. The radial distribution function (RDF) in real space was then obtained via Fourier transformation of the EXAFS data in k space. A 1–6 \AA range was used for displaying the RDFs. Theoretical phases and amplitudes for each element were calculated by the FEFF7 program. Fitted structural parameters were then obtained using the calculated amplitudes and phases for each coordination shell. Because the structural parameters for the first coordination shell usually can be analyzed with high accuracy, we employed Fourier filtering by Fourier transforming the first major peak in the RDF to k space (3.5–11 \AA^{-1}) to obtain the filtered EXAFS data. The filtering window was set to be 1 to 3 \AA , and a 0.2- \AA slope was used to reduce ripples caused by Fourier filtering. An optimization program in the EXAFSPAK package

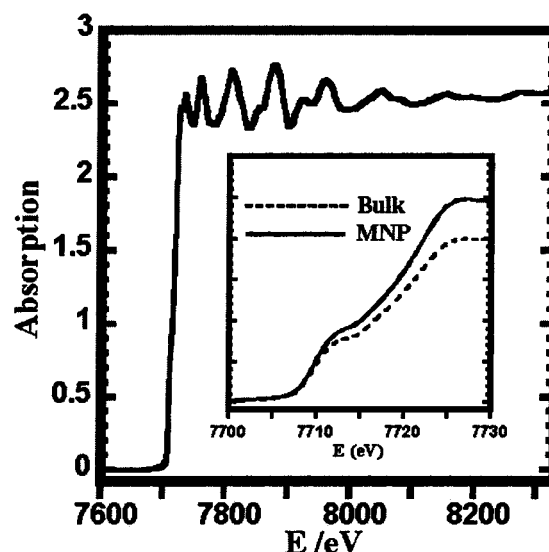


Figure 1. EXAFS measurement on Co in the bi-MNP sample. The insert shows the near edge curves of Co in the bulk and bi-MNPs. The signal corresponding to Co oxides in the preedge region is below the detectable level.

was then used to fit these data to obtain the fitted parameters. The aforementioned k range was so chosen to minimize the distortion caused by the Co fluorescence on the Ni EXAFS measurements because the K edges of Ni and Co are only 624 eV apart. The distortion produced by the Co K line fluorescence on the low energy portion of the Ni EXAFS spectrum was estimated to be less than 3% because of the lack of modulation of Co fluorescence (EXAFS) in this region. When the Ge detector was used, the amount of distortion was reduced by over an order of magnitude, making the error negligible. It is also worth pointing out that after the fitting, the amplitudes of the Fourier transform were higher than the original ones due to the reduction in the range of data in real space. However, since the parameter fitting process was actually performed in k space, no distortion was introduced by this procedure. After fitting, three parameters, N (coordination number), σ (disorder or the Debye–Waller factor), and R (bond distances), defining the first coordination shell were obtained.

Error analysis was carried out to estimate the standard deviation for the fitted parameters. An effective way was to use the error (the F value) in the EXAFSPAK package. The standard deviation of a specific fitting parameter was obtained when the F value was doubled while changing that parameter.²⁹ This method is compatible to the χ^2 method, in which the experimental errors as noise are included.³⁰ We found that $F \leq 100$ generally corresponded to a good fitting as indicated by the χ^2 method, after considering the experimental noise in our EXAFS data.

High-resolution TEM (JEOL JEM-200 CX operated at 200 keV) was used to perform selected area diffraction and (SAD) and dark field imaging measurements on these nanoparticles at the National Center for Electron Microscopy (NCEM) at Berkeley. Micro-micro diffraction was also taken on individual nanoparticles. The composition of these particles on an individual nanoparticle basis was measured using energy-dispersive X-ray spectroscopy (EDX) with the TEM.

Results and Discussion

Figure 1 shows the EXAFS curve of Co in Ni/Co bi-MNPs after background correction. EXAFS measurements on the Co and Ni standards, and on Ni in bi-MNPs have yielded similar

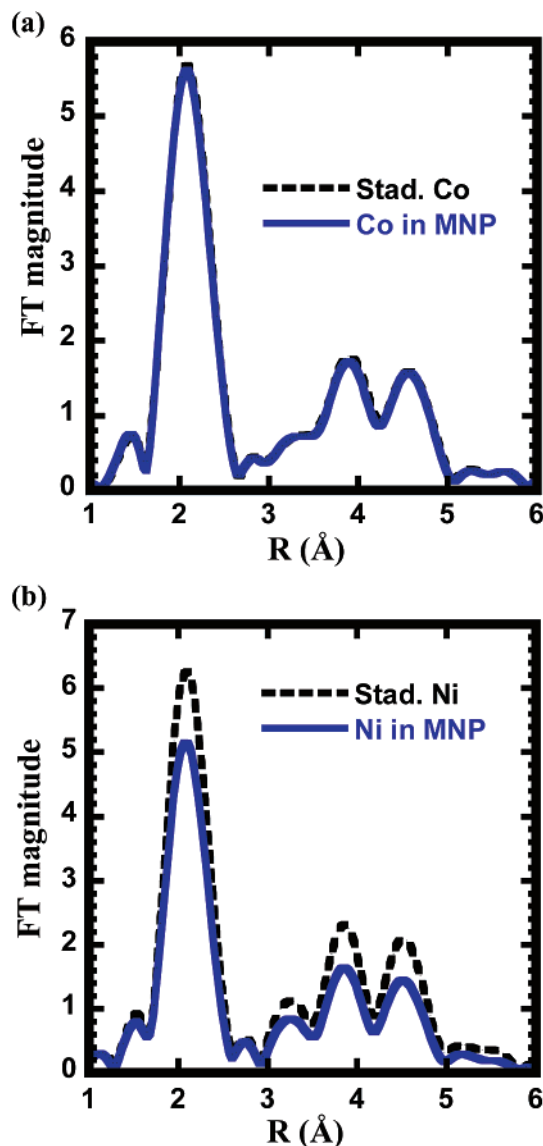


Figure 2. Fourier transforms of EXAFS data of Co in the bi-MNP sample (solid line) and the standard (dashed line) (a), and Ni in the bi-MNP sample (solid line) and the standard (dashed line) (b). EXAFS data between 3.5 and 11 \AA^{-1} is Fourier transformed to the RDFs shown here.

results. The insert in Figure 1 shows the near edge patterns of Co in bi-MNPs (solid line) and the bulk (dashed line). It is evident that the metals in the SWNT samples are oxide free, as indicated by the lack of the metal–oxygen preedge peaks. Since the magnitude of the jumps in the absorption spectra of Ni and Co at the K edge are approximately the same (not shown), there should be approximately equal amounts of Ni and Co in the bi-MNP sample. The results of EXAFS measurements on the standards are similar to the those obtained previously at room temperature,³¹ all showing that the modulation in Co EXAFS is slightly smaller than that of Ni.

Figure 2 shows Fourier transforms (phase uncorrected) of these EXAFS profiles after data processing. Peaks in RDFs represent different coordination shells, and the profiles of these peaks are determined by the local atomic arrangement. The lack of oxides is also clearly shown in the Fourier transforms because of the missing intensity near 1.5 \AA (phase uncorrected). The peaks at 1.5 \AA (phase uncorrected) in Figure 2 correspond to a sideband of metal–metal scattering. The missing of oxides may be due to the fact that all the particles are protected by multiple

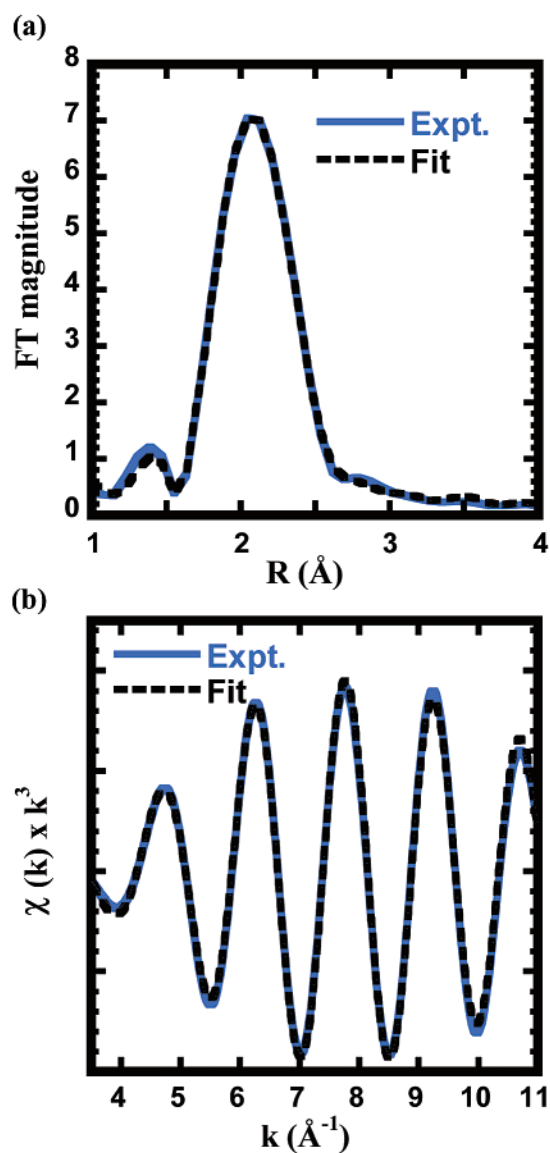


Figure 3. Fourier transforms of Fourier filtered first coordination shell for the Co in the bi-MNPs and the fitted one (a), and the Co EXAFS data and fitted curve (b). The single scattering theory is used, and phase-uncorrected Fourier transforms of the EXAFS data are also shown. The optimized fitting parameters with phase correction are listed in Table 1.

layers of graphite, as observed in other TEM investigations,¹⁴ suggesting that magnetic particles made in a similar manner should also be stable in air.

From Figure 2, it is apparent that the local environment around the Ni atoms in the bi-MNPs is different from that of Ni in the bulk. For Co, the RDF of the Co in bi-MNPs is almost identical to that of the bulk. Although this result suggests that the Co atoms reside in an environment that is very close to the bulk, as we will show below, the explanation is actually more complex. Nonetheless, the difference between the local environments of Ni and Co in the bi-MNPs is obvious.

Using the single scattering theory together with Fourier filtering, fitting parameters are obtained for all the first coordination shells. Figure 3 shows the filtered (solid lines) and fitted data (dashed lines) for the Co in the bi-MNPs in both real (Figure 3a) and k space (Figure 3b), and the obtained fitting parameters are listed in Table 1. Results of Ni in bi-MNPs (Figure 4a) and in the bulk (Figure 4b) are shown in Figure 4. Since both Ni and Co are in the bi-MNP, the backscattering

TABLE 1: Fitted Parameters for the First Coordination Shells of Ni and Co in Bi-MNPs^a

materials	S_0	N	$R(\text{\AA})$	σ^2
Ni standard	0.682	12.0 (0.6)	2.469 (0.002)	0.00538 (0.00027)
Co standard	0.690	12.0 (0.6)	2.478 (0.003)	0.00590 (0.00037)
Ni in bi-MNPs (Ni–Ni)	0.682	5.6 (0.4)	2.469 (0.005)	0.00532 (0.00054)
Ni in bi-MNPs (Ni–Co)	0.682	4.4 (0.5)	2.473 (0.006)	0.00541 (0.00089)
Co in bi-MNPs (Co–Co)	0.690	6.6 (0.5)	2.466 (0.005)	0.00538 (0.00059)
Co in bi-MNPs (Co–Ni)	0.690	4.4 (0.5)	2.473 (0.006)	0.00541 (0.00089)

^a S_0 is the scaling factor, R is the bond distance, σ is the Debye–Waller factor, and N is the coordination number. The standard deviations are shown in parentheses.

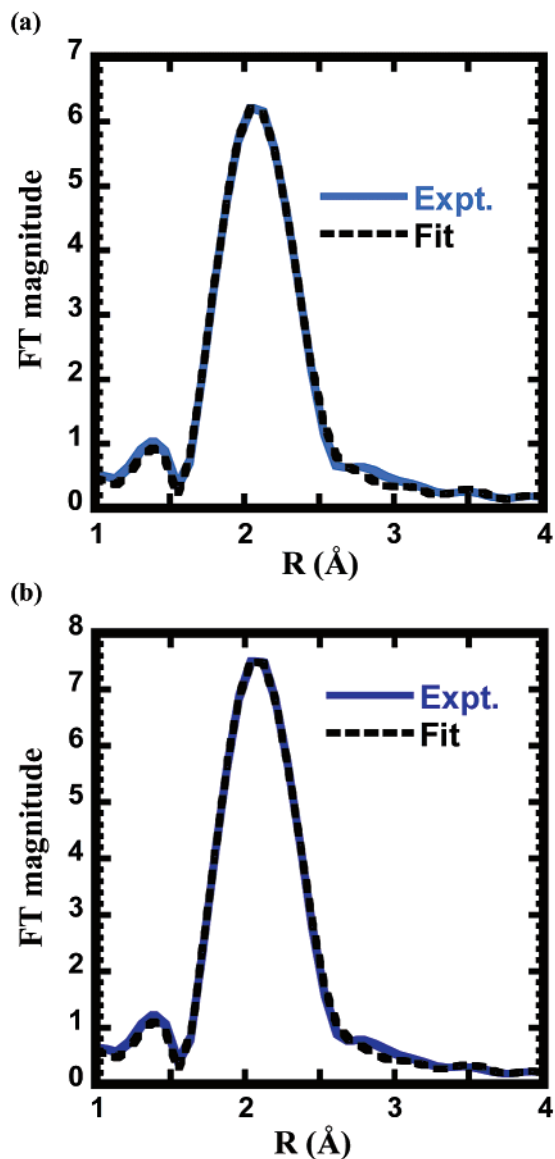


Figure 4. Fourier transforms of Fourier filtered first coordination shells for Ni in the bi-MNPs (a) and the bulk (b). Conditions for the fitting are identical to those described in Figure 3.

atoms include both Ni and Co. Consequently the first coordination shell consists of both Ni–Ni and Ni–Co for an absorbing Ni atom, and Co–Co and Co–Ni for an absorbing Co atom. The optimal Ni–Co coordination number, which should be the same in the first shells for Ni and Co in the bi-MNPs, is obtained by scanning this coordination number from 1 to 9 while minimizing the combined error in the fittings for both Ni and Co in bi-MNPs. During the fitting, the disorders (σ), coordination numbers (N), bond distances (R), and E_0 are varied. From Table 1, it is obvious that Ni atoms in bi-MNPs have fewer neighbors (10.0) than the Co atoms do (11.0). In addition, Co

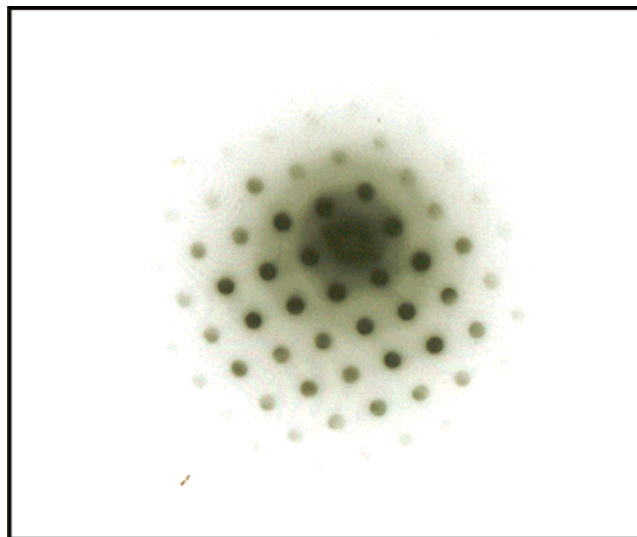


Figure 5. Electron diffraction (ED) pattern of a single bi-MNP. The pattern fits well to a Ni or Co fcc (011) ($a = 3.5 \text{ \AA}$) structure.

has more Co as nearest neighbors (6.6) than the Ni does (4.4), although in bulk these two elements are totally miscible.³² The results from the Ge detector are similar to those shown in Table 1, except the coordination numbers are slightly lower. On the basis of the first coordination numbers of Co and Ni, the average size of these nanoparticles is determined to be 3.0 nm.

The squares of disorder (σ^2) for the Co and Ni in the bi-MNPs and that for Ni in the bulk shown in Table 1 are very similar. The disorder for the Co in the bulk is slightly higher. This suggests that both Ni and Co in the bi-MNPs are in similarly ordered structures, which are also close to that of the Ni bulk. The slight decrease in disorder for Co in the bi-MNPs may be caused by the extensive mixing of Ni and Co, which makes Co slightly more ordered than they are in the bulk. Although it is well-known that the surface atoms in some of the small MNPs (1–2 nm) have larger disorders, it is apparently not the case for the Ni/Co bi-MNPs in the soot, based on the EXAFS and TEM measurements. The observation that the majority of the MNPs are highly ordered is also supported by the results of selected area diffraction (SAD) and dark field imaging measurements in which crystalline nanoparticles are observed. Micro-micro diffraction has been performed on individual nanoparticles, and the result is shown in Figure 5. The pattern fits well to a Ni or Co fcc (011) ($a = 3.5 \text{ \AA}$) structure.

The sizes of the particles in the bi-MNP/SWNT sample have also been estimated with TEM. Figure 6 shows the size distribution of over 430 particles. It is worth remarking that TEM is a sampling technique, i.e., only those which are visible to TEM can be measured. On the other hand, EXAFS measures all the material in a sample. It is possible that many particles, especially the small ones that are obscured by other materials, are not included in the counting. The disparity between this

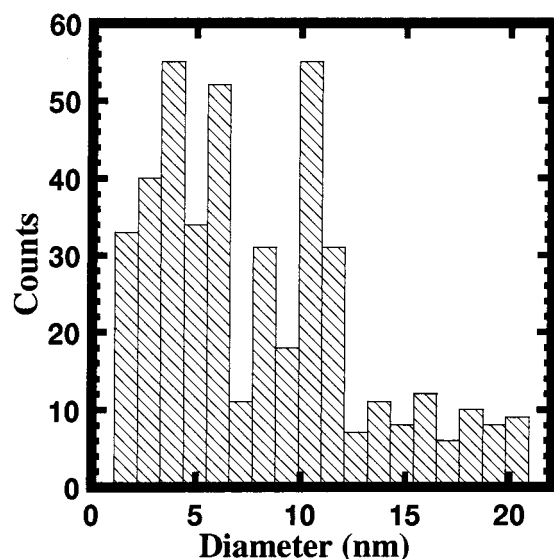


Figure 6. The size distribution of particles by bright-field TEM measurements. The average size is 8 nm with a standard deviation of 5 nm.

result (8.0 ± 5.0 nm) and the one obtained based on EXAFS measurements (3.0 nm) is obvious. It shows that a large number of small particles may be missed in the TEM measurement.

The results of the TEM dark field imaging are shown in Figure 7b. Because only the portions that have the (111) plane orientation in those crystalline particles are visible in the dark field, the average size of particles obtained from the dark field (5.0 ± 3.0 nm) is smaller than that obtained from the bright field measurements (8.0 ± 5.0 nm), which are shown in Figure 7a. The difference between the two average sizes may be explained by the multiple domains existing in those particles.

We have measured the composition of these particles on an individual nanoparticle basis. Samples are examined with EDX to determine the composition of individual particles. Figure 8a shows a typical image of the raw material. Figure 8b displays the result of the EDX analysis of the single particle selected in Figure 8a, as pointed at by the arrow. We have examined totally 20 particles of different sizes, and the average ratio of the amount of Co to Ni in these particles is $50 \pm 5\%:50 \pm 5\%$.

Discussion

Those results can be explained in three possible ways. First, since the disorders are similar for Ni and Co atoms in those nanoparticles, the lower coordination number for Ni can only mean that more Ni atoms are in the surface. For example, nanoparticles of 3.0-nm diameter containing equal amounts of Ni and Co have on average 10.5 nearest neighbors.³³ On the other hand, this number is 9.0 for Ni and 12.0 for Co for the same size bi-MNPs with all the surface atoms being Ni. Clearly, the real structure lies somewhere between the full segregation model and the totally uniform bi-MNPs.

The second explanation can be that there are more isolated Ni atoms in the soot since such an arrangement can effectively lower the coordination number for Ni. However, this is unlikely for two reasons. First, if many Ni are in the atomic form, they could be easily oxidized, and these oxides should be visible in the EXAFS measurements. (Although one may argue that it should be possible to tell whether carbides exist by examining the metal-carbon peak in EXAFS, we must point out that it is difficult to tell whether the surface is passivated with carbon based on EXAFS data since the backscattering amplitude of

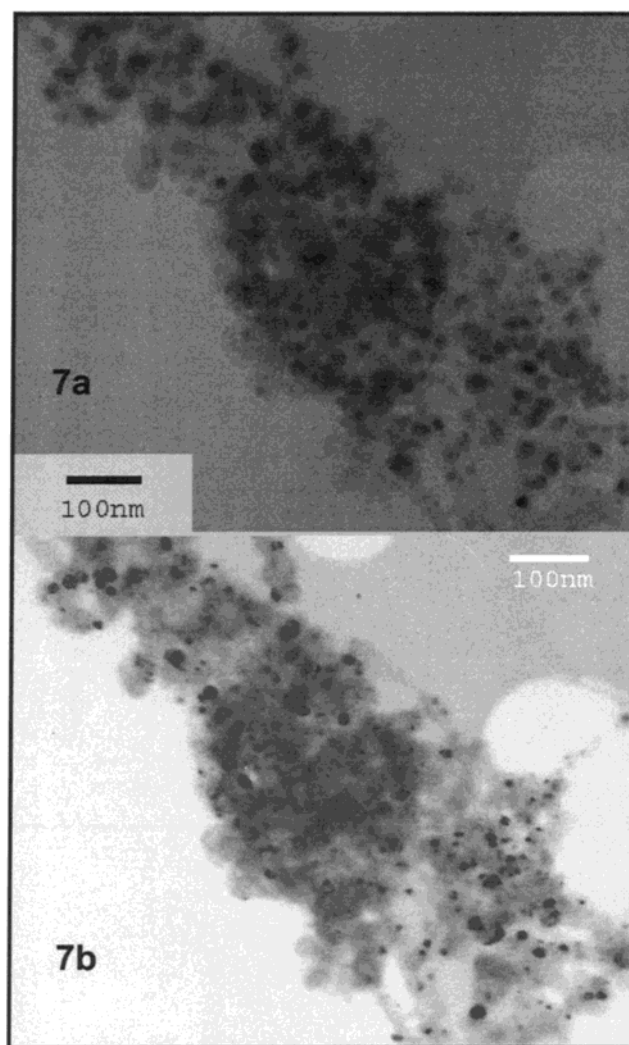


Figure 7. Bright and dark field (detecting only the (111) plane) images of the bi-MNPs. The average sizes of the bi-MNPs in these two pictures are 8.0 ± 5.0 nm for bright-field imaging, and 5.0 ± 3.0 nm for dark-field imaging, indicating that the majority of the particles are highly ordered since the dark field can only probe crystalline samples.

carbon is weak. Furthermore, the overlap between the main peak in the Ni-C RDF curve and that of the sideband from Ni-Ni at ~ 1.4 Å (phase uncorrected, see Figure 2) makes it difficult to predict the amount of metal carbide in the sample.). Second, TEM data shows that there are equal amounts of Co and Ni in all the particles examined, as shown in Figure 8. That microscopic finding agrees with the X-ray absorption measurements shown earlier, which probe several micrograms of the similar material that contains millions of nanoparticles. All these results support the notion that all Ni and Co are in the bi-MNP form.

The last possible scenario is that the Ni portion in the bi-MNPs has more defects than that of Co. However, as the disorders and dark field images have indicated, both metals are similarly structured. Therefore, it is unlikely that the Ni portion has more defects.

We have simulated different Ni/Co bi-MNPs with carbon on the surface, and have compared them with the experimental data. Figure 9a shows the results of the simulation for Co. It contains the Fourier transforms of the EXAFS data of the Co bulk (fcc), pure Co MNPs, uniform Co/Ni bi-MNPs, and surface segregated Co/Ni bi-MNPs. In the simulation, we assume the disorders for Co in all those samples are the same with the exception of Co

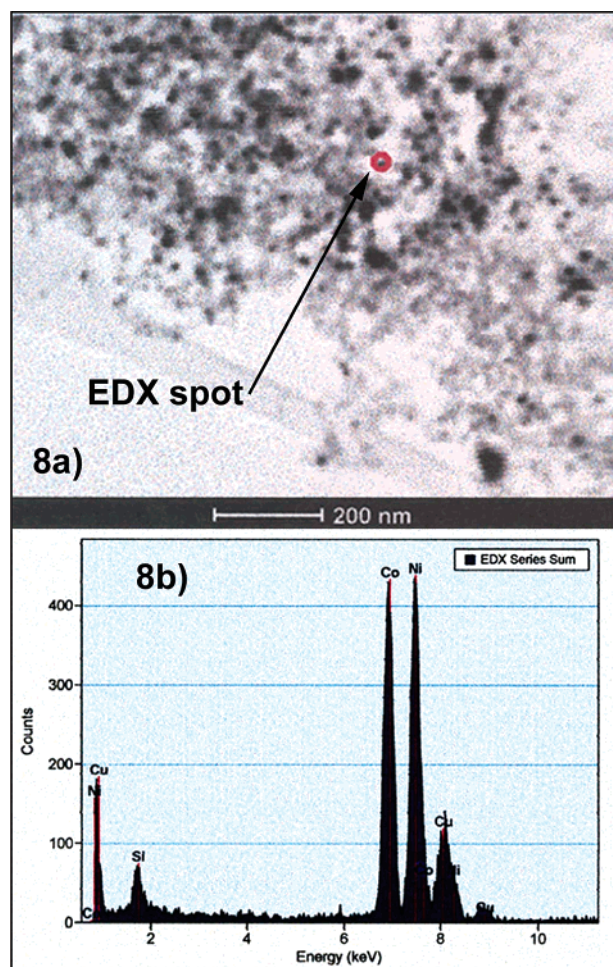


Figure 8. TEM image (a) and energy-dispersive X-ray analysis (EDX) (b) of a single MNP (shown in (a) by the arrow). The Cu signal originated from the Cu grids. The size of the particle probed here is ~ 10 nm.

bulk, in which a higher value based on the measurements is used. The average size of MNPs is 3 nm. The results shown in Figure 9a suggest that only the surface segregated Co/Ni bi-MNPs can duplicate the measured result, which was identical to the EXAFS data of the bulk. Similar calculations have been performed on Ni, and the correct model is again the surface segregated Co/Ni bi-MNPs. The results are shown in Figure 9b.

On the basis of the experimental results and simulation, we propose that bi-MNPs have more Ni atoms in the surface and more Co atoms on the inside. This model allows us to explain all the observations and the fitted parameters. The reason that the Co in the sample produces an EXAFS similar to that for Co bulk is because the Co atoms are slightly more ordered in the bi-MNPs, and the majority of Co are on the inside of Ni/Co bi-MNPs. In the same vein, the modulation in the EXAFS of Ni is lower because of the large number of surface atoms, which have fewer nearest neighbors.

The observed segregation effect can be partially attributed to the lowering of surface energy due to the Ni atoms in the surface.³⁴ If this is the dominant cause, then particles of smaller sizes should experience an even stronger surface segregation effect due to the higher percentage of surface atoms. For example, the percentage of surface atoms increases to above 50% when the size of bi-MNPs becomes smaller than 2.5 nm. Furthermore, since the average diameter of SWNTs synthesized in this manner is usually 1.6 ± 0.5 nm, the Co/Ni bi-MNPs in

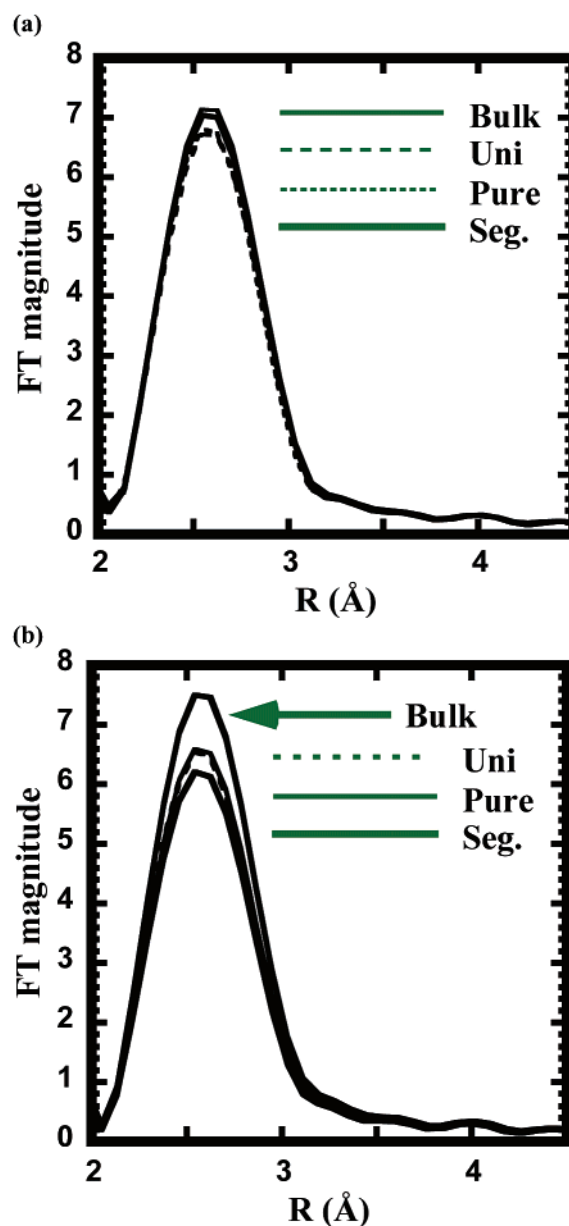


Figure 9. (a) Simulation results of Co bulk (solid line), pure Co MNPs (dotted line), uniformly mixed Co/Ni MNPs (dashed line), and surface segregated Co/Ni MNPs (solid line). Note that the Co bulk and surface segregated model produce similar RDF profiles. (b) Simulation results for Ni. Note that the amplitude of the RDF for surface segregated model is $\sim 20\%$ lower than that of the bulk, nearly reproducing the experimental results shown in Figure 2. The size of the MNPs is 3 nm.

the 1–2 nm diameter range should be responsible for their growth. In this case, the percentage of the surface atoms can be over 75%. This means that all the core atoms are Co, and both Co and Ni are in the surface, although Ni dominates. Such a segregated arrangement may create an optimized environment for the growth of SWNTs. If this is true, then the size of the nanoparticles controls the surface composition and, consequently, the chemical properties of those metal nanoparticles.

Because the yield of SWNTs is usually strong temperature dependent, it is desirable to measure the structures of bi-MNPs produced at different temperatures, including room temperature. Further investigations are also necessary to learn more about the structures of these nanoparticles at high temperatures to determine whether these nanoparticles retain the surface segregated structure at the growth temperature of > 800 °C. These

measurements are being planned according to the availability of the synchrotron beam time soon.

Conclusion

We have investigated bi-MNPs with EXAFS spectroscopy and TEM. It is found that these bi-MNPs are highly ordered, are made of equal amounts of Ni and Co, and are covered with mainly Ni atoms. The average size measured by EXAFS is 3 nm, although this value is different from that obtained from TEM data, which is 8 nm. This implies that many particles are too small to be visible to even high-resolution TEM. Our findings suggest that the structure factor may play an important role in the growth mechanisms of SWNT.

Acknowledgment. We thank Chuck Echer at the National Center for Electron Microscope (NCEM), and the excellent staff at Stanford Synchrotron Radiation Laboratory (SSRL) for experimental support. We also are grateful to DOE for support of both facilities. Acknowledgment is made to the donors of the Petroleum Research Fund, administered by the American Chemical Society, for partial support of this research. This work is also partially supported by the Camille and Henry Dreyfus Foundation.

References and Notes

- (1) Rousset, J. L.; Aires, F.; Bornette, F.; Cattenot, M.; Pellarin, M.; Stievano, L.; Renouprez, A. *J. Appl. Surf. Sci.* **2000**, *164*, 163–168.
- (2) Sinfelt, J. H. *Bimetallic catalysts: discoveries, concepts, and applications*; Wiley: New York, 1983.
- (3) Baker, R. T. *Carbon* **1989**, *27*, 315.
- (4) Iijima, S.; Ichihashi, T. *Nature* **1993**, *364*, 737–737.
- (5) Bethune, D. S.; Kiang, C. H.; Devries, M. S.; Gorman, G.; Savoy, R.; Vazquez, J.; Beyers, R. *Nature* **1993**, *363*, 605–607.
- (6) Guo, T.; Nikolaev, P.; Thess, A.; Colbert, D. T.; Smalley, R. E. *Chem. Phys. Lett.* **1995**, *243*, 49–54.
- (7) Geohegan, D. B.; Schittenhelm, H.; Fan, X.; Pennycook, S. J.; Poretzky, A. A.; Guillorn, M. A.; Blom, D. A.; Joy, D. C. *Appl. Phys. Lett.* **2001**, *78*, 3307–3309.
- (8) Fiermans, L.; De Gryse, R.; De Doncker, G.; Jacobs, P. A.; Martens, J. A. *J. Catal.* **2000**, *193*, 108–114.
- (9) Yasuda, H.; Matsubayashi, N.; Sato, T.; Yoshimura, Y. *Catal. Lett.* **1998**, *54*, 23–27.
- (10) Kumeda, Y.; Fukuhira, Y.; Taketsugu, T.; Hirano, T. *Chem. Phys. Lett.* **2001**, *333*, 29–35.
- (11) Cornwell, C. F.; Wille, L. T. *J. Chem. Phys.* **1998**, *109*, 763–767.
- (12) Bronikowski, M. J.; Willis, P. A.; Colbert, D. T.; Smith, K. A.; Smalley, R. E. *J. Vac. Sci. Technol., A—Vacuum Surfaces Films* **2001**, *19*, 1800–1805.
- (13) Kitamura, N.; Oshiyama, A. *J. Phys. Soc. Jpn.* **2001**, *70*, 1995–2011.
- (14) Jiao, J.; Seraphin, S. *J. Phys. Chem. Solids* **2000**, *61*, 1055–1067.
- (15) Nikolaev, P.; Bronikowski, M. J.; Bradley, R. K.; Rohmund, F.; Colbert, D. T.; Smith, K. A.; Smalley, R. E. *Chem. Phys. Lett.* **1999**, *313*, 91–97.
- (16) Kokai, F.; Takahashi, K.; Yudasaka, M.; Yamada, R.; Ichihashi, T.; Iijima, S. *J. Phys. Chem. B* **1999**, *103*, 4346–4351.
- (17) Hafner, J. H.; Bronikowski, M. J.; Azamian, B. R.; Nikolaev, P.; Rinzler, A. G.; Colbert, D. T.; Smith, K. A.; Smalley, R. E. *Chem. Phys. Lett.* **1998**, *296*, 195–202.
- (18) Lee, Y. H.; Kim, S. G.; Tomanek, D. *Phys. Rev. Lett.* **1997**, *78*, 2393–2396.
- (19) Maiti, A.; Brabec, C. J.; Bernholc, J. *Phys. Rev. B—Condensed Matter* **1997**, *55*, R6097–R6100.
- (20) Dai, H. J.; Rinzler, A. G.; Nikolaev, P.; Thess, A.; Colbert, D. T.; Smalley, R. E. *Chem. Phys. Lett.* **1996**, *260*, 471–475.
- (21) Brabec, C. J.; Maiti, A.; Roland, C.; Bernholc, J. *Chem. Phys. Lett.* **1995**, *236*, 150–155.
- (22) Seraphin, S.; Zhou, D. *Appl. Phys. Lett.* **1994**, *64*, 2087–2089.
- (23) Sen, R.; Ohtsuka, Y.; Ishigaki, T.; Kasuya, D.; Suzuki, S.; Kataura, H.; Achiba, Y. *Chem. Phys. Lett.* **2000**, *332*, 467–473.
- (24) Takizawa, M.; Bandow, S.; Yudasaka, M.; Ando, Y.; Shimoyama, H.; Iijima, S. *Chem. Phys. Lett.* **2000**, *326*, 351–357.
- (25) Kiang, C. H. *J. Phys. Chem. A* **2000**, *104*, 2454–2456.
- (26) Charlier, J. C.; DeVita, A.; Blase, X.; Car, R. *Science* **1997**, *275*, 646–649.
- (27) Thess, A.; Lee, R.; Nikolaev, P.; Dai, H. J.; Petit, P.; Robert, J.; Xu, C. H.; Lee, Y. H.; Kim, S. G.; Rinzler, A. G.; Colbert, D. T.; Scuseria, G. E.; Tomanek, D.; Fischer, J. E.; Smalley, R. E. *Science* **1996**, *273*, 483–487.
- (28) Ankudinov, A. L.; Ravel, B.; Rehr, J. J.; Conradson, S. D. *Phys. Rev. B—Condensed Matter* **1998**, *58*, 7565–7576.
- (29) Hosokawa, H.; Fujiwara, H.; Murakoshi, K.; Wada, Y.; Yanagida, S.; Satoh, M. *J. Phys. Chem.* **1996**, *100*, 6649–6656.
- (30) Lytle, F. W.; Sayers, D. E.; Stern, E. A. *Physica B* **1989**, *158*, 701–722.
- (31) ftp://xafs.chem.msu.su/data/Farrel_Lytle_data/.
- (32) Massalski, T. B.; Okamoto, H.; *ASM International, Binary alloy phase diagrams*, 2nd ed.; ASM International: Materials Park, OH, 1990.
- (33) Benfield, R. E. *J. Chem. Soc., Faraday Trans.* **1992**, *88*, 1107–1110.
- (34) Poncet, V.; Bond, G. C. *Catalysis by metals and alloys*; Elsevier: Amsterdam; New York, 1995.